


Magnetometry Based on Silicon-Vacancy Centers in Isotopically Purified 4H-SiC

I. Lekavicius^{1,*}, S.G. Carter,^{1,†} D.J. Pennachio¹, S. White², J.R. Hajzus³, A.P. Purdy,¹
D.K. Gaskill,^{1,‡} A.L. Yeats,¹ and R.L. Myers-Ward¹

¹*US Naval Research Laboratory, Washington, DC 20375, USA*

²*NRC Research Associate at the US Naval Research Laboratory, Washington, DC 20375, USA*

³*ASEE Research Associate at the US Naval Research Laboratory, Washington, DC 20375, USA*

 (Received 19 December 2022; revised 13 February 2023; accepted 24 March 2023; published 27 April 2023; corrected 10 May 2023)

Point defects in solid-state materials are promising systems in the fields of quantum information, communications, and sensing. Particular to sensing, defects with coherent spin states are used for high-sensitivity room-temperature sensing under ambient conditions. Applications involving magnetic sensing with point defects are mostly dominated by the nitrogen-vacancy center in diamond, which possesses an attractive combination of spin coherence at room temperature as well as spin initialization and read-out. However, spin defects in other materials are explored as alternatives, especially in industrially mature materials, such as silicon carbide. Here, we report on the improved sensitivity of a magnetic sensor system utilizing an ensemble of silicon vacancies in silicon carbide due to isotopic purification of the host crystal. A maximum sensitivity of 4.0 nT/ $\sqrt{\text{Hz}}$ is reported, representing an order of magnitude improvement from the best previously reported sensitivity. Additional sensing modalities, such as angle-resolved magnetic imaging and highly broadband ac field sensing, are also demonstrated.

DOI: [10.1103/PhysRevApplied.19.044086](https://doi.org/10.1103/PhysRevApplied.19.044086)

I. INTRODUCTION

Transitions between spin states are naturally suited for applications in magnetic sensing due to their energy-level dependence on external magnetic fields. Common implementations to exploit these transitions use an ensemble of atoms, such as atomic vapor cells [1], but much attention is also given to point defects in solid-state materials. Some of these defects combine room-temperature and ambient-condition operation with extremely short working distances between the sensor and the target. The practical advantages of these systems come at the cost of reduced coherence of the spin transitions, due to the presence of a magnetically noisy solid-state environment. As such, particular focus is on reducing the abundance of nuclear-spin-carrying isotopes of the host crystal of the defect. The majority of applications involving sensing with these defects utilize the nitrogen-vacancy (N-V) center in isotopically purified [2–4] diamond, which possesses a spin state that is coherent at room temperature and can be initialized and read out optically with an off-resonant laser

drive [5]. These properties lead to the application of the diamond N-V magnetometer in sensing biological samples [6–8], high-spatial-resolution NMR [9,10], geological samples [11], and in condensed matter samples [12].

Defects in silicon carbide, such as the silicon vacancy [13–15] and the various configurations of the divacancy [16,17], are explored as alternatives to the N-V center in diamond. Silicon carbide possesses attractive properties such as chemical inertness, a large band gap, and optimal acoustic properties, while also being a material with high- $\chi^{(2)}$ and $-\chi^{(3)}$ parameters. In addition, the manufacture and fabrication of silicon carbide is much more industrially mature than that of diamond, which is especially important in terms of the fabrication of high-quality photonic structures [18,19] and diode fabrication for charge-state stabilization of color centers [20]. The silicon vacancy, in particular, is shown to have accessible room-temperature spin transitions, which are used for magnetic sensing [21,22]. Of particular note are previously demonstrated sensing schemes with all-electrical read-out of the spin states [23], as well as all-optically-driven measurements of the spins in isotopically enriched silicon carbide [24]. There are many polytypes of silicon carbide, and in each polytype, there are a number of inequivalent lattice sites where a single silicon monovacancy can reside. This work focuses exclusively on the V2 center in 4H-SiC, one of two nonequivalent silicon-vacancy sites in the 4H polytype. The V2 center has a zero-phonon line emitting at 916 nm [25] and a

*ignas.lekavicius@nrl.navy.mil

[†]Current affiliation: Laboratory for Physical Sciences, College Park, Maryland, 20740, USA

[‡]Current affiliation: Institute for Research in Electronics and Applied Physics, University of Maryland, College Park, Maryland, 20742, USA

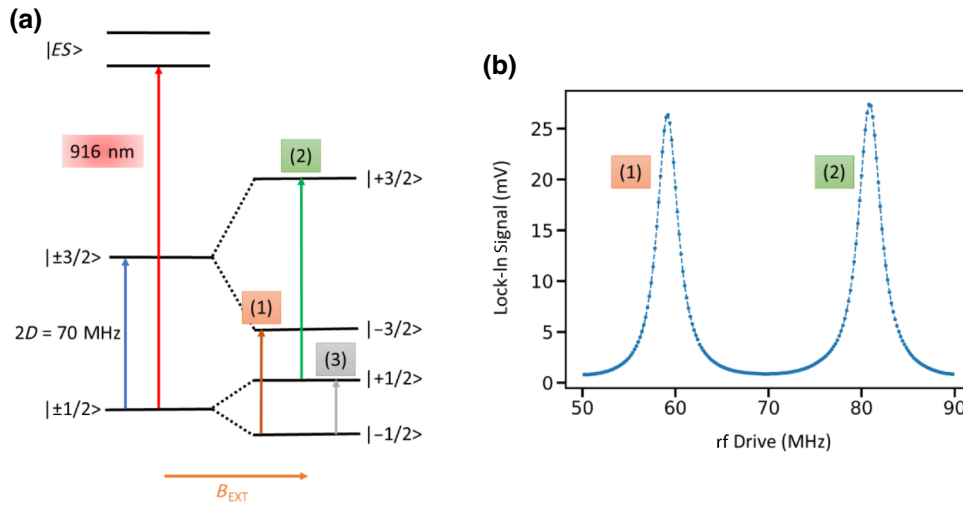


FIG. 1. Energy-level structure and ODMR. (a) Spin-quartet ground state of the V_2 center, with the allowed $\Delta m = 1$ transitions labeled 1–3. (b) Typical ODMR scan at an external-magnetic-field-induced Zeeman splitting of about 10 MHz. Transitions 1 and 2 are labeled in accordance with (a).

$S = 3/2$ ground-state spin quartet with a zero-field splitting (ZFS) $2D = 70$ MHz (Fig. 1(a), blue arrow), which is measured at room temperature via optically detected magnetic resonance (ODMR). The room-temperature ODMR measurement relies on spin initialization and read-out made possible by a spin-dependent intersystem crossing [26], meaning the excited states have different probabilities of nonradiatively relaxing to their respective spin ground states. This results in a photoluminescence (PL) intensity difference based on the initial spin state and optically induced spin initialization after a few excitation cycles.

The coherence time of the spin transitions is of critical importance in the applications of magnetic sensing due to its role in both continuous wave (cw) and pulsed magnetic sensing schemes [27]. Of particular interest is the inhomogeneous dephasing time, T_2^* , which limits the sensitivity of dc sensing of solid-state magnetometers. As shown with the N- V center, one of the dominant sources of decoherence is the fluctuating magnetic field from the nuclear-spin-carrying isotopes of the host crystal [28], which, in the case of silicon carbide, are ^{29}Si and ^{13}C . Previous work showed that the T_2^* of a V_2 ensemble could exceed $20 \mu\text{s}$ in an isotopically pure $4H$ -SiC lattice using a strain-independent basis in the ground-state quartet [29]. In addition, the symmetry axis of all V_2 centers is oriented along the c axis of the silicon carbide crystal, which is (nearly) out of the plane of the silicon carbide wafer for our $4H$ -SiC cut. This is in contrast to the N- V center in diamond, which can be found oriented in one of four distinct $\langle 111 \rangle$ directions in the diamond lattice. The V_2 system, therefore, offers improved contrast and sensitivity of magnetic measurements, since all defects have the same magnetic field projection along their axis, but these advantages come at the cost of losing vector magnetometry capabilities (excluding operations at the magic angle [30]). However, it has been pointed out that, due to the relatively low ZFS of the V_2 center, the amplitude of the

off-axis magnetic field can be measured in the low-field regime in addition to the on-axis component [30,31]. An implementation of this type of angle-resolved magnetic imaging is demonstrated in this work. The two transitions, $|-1/2\rangle \rightarrow |-3/2\rangle$ and $|1/2\rangle \rightarrow |3/2\rangle$, labeled (1) and (2), respectively, in Fig. 1(a), can be measured simultaneously and independently. This gives a way to effectively double the contrast of magnetic sensing. Moreover, in the regime of a mostly axial magnetic field, orthogonal linear combinations of these two transition frequencies give the values of the ZFS and the Zeeman splitting. The Zeeman splitting is solely sensitive to magnetic fields, while the ZFS is sensitive to strain, meaning simultaneous sensing modalities are possible with this system.

II. SETUP

Here, we use similar samples as in our previous work [29], with a $20\text{-}\mu\text{m}$ -thick isotopically enriched epilayer, with ^{29}Si and ^{13}C concentrations reduced from $4.7\% \rightarrow 0.01\%$ and $1.1\% \rightarrow 0.15\%$, respectively, grown on a $500\text{-}\mu\text{m}$ N + $4H$ -SiC commercially available substrate (II-VI Inc.). The sample is electron irradiated at 1 MeV with a dose of $3 \times 10^{19} e^-/\text{cm}^2$ and then annealed in air at 700°C for 2 h. The experimental setup for the magnetometer is shown in Fig. 2. An 800-nm Ti:sapphire laser is passed through a noise eater, gated by an acousto-optic modulator (AOM), and then reflected on a dichroic beamsplitter. The beam is then passed through a cylindrical lens and onto a right-angle mirror, which reflects the beam onto the side of the silicon carbide sample, illuminating the epilayer with an area approximately $200 \times 20 \mu\text{m}^2$. The PL, which emits primarily perpendicular to the c axis of the silicon carbide, follows the same optical path back to the dichroic mirror, at which point it transmits through. A second dichroic mirror picks off the laser leakage into the reference path of an autobalanced photodiode, while

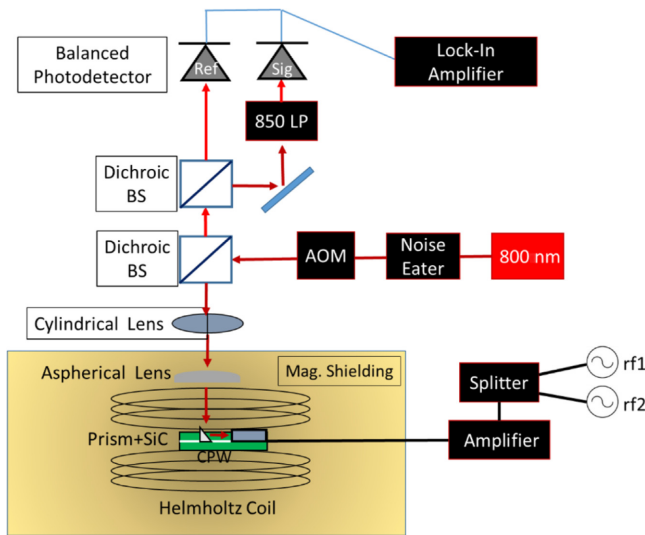


FIG. 2. Measurement setup for ODMR and Ramsey experiments. 800-nm laser and rf sources are used to initialize and drive spin transitions in a magnetically shielded SiC sample. PL emission is collected from the side of the SiC sample and filtered onto a balanced photodiode, the signal of which is sent to a lock-in amplifier. LP corresponds to long pass.

the PL continues to the signal port of the photodiode. The signal from the photodiode is then sent to a lock-in amplifier. The sample sits atop a printed-circuit-board coplanar waveguide (CPW) with a 1-mm central strip line connected to two amplified rf generators for the resonant addressing of the spin transitions. The sample and coplanar waveguide are situated at the center of a Helmholtz coil for the generation of a spatially uniform magnetic field to split the otherwise degenerate transitions in the spin quartet. A custom magnetic shield (CONETIC AA .006”) surrounds the coil and sample to reduce the amplitude of stray magnetic fields from the environment.

III. ODMR SENSITIVITY

An ODMR scan is shown in Fig. 1(b), where the rf field is amplitude modulated at 700 Hz and 100% depth, with the lock-in amplifier detecting the difference between PL with and without the rf field being present. In the interest of removing any dependence on drift in the signal amplitude, we frequency modulate to get a feature centered around 0 mV [Fig. 3(a)]. This feature is used as an error signal in a software-based feedback loop for tracking the transition of interest with high dynamic range. The slope in the linear region of Fig. 3(a) is of critical importance to the sensitivity, as it determines the conversion of the lock-in voltage to the external magnetic field amplitude. Figure 3(b) shows real-time tracking data of rf-drive ω_1 locked onto transition 1 as the magnetic field from the Helmholtz coil is stepped in 35 nT increments.

The presence of two transitions with independent spin populations in the $V/2$ center can be exploited to both increase the contrast of the measurement and decouple the effects of the magnetic field from strain. These separate transitions can be measured on the X and Y quadratures of the lock-in amplifier if the modulation function for the rf drives of the respective transitions is given a relative phase offset of $\pi/2$ [Fig. 3(c)]. Assuming the magnetic field is primarily along the c axis, the linear combinations, $(\omega_1 + \omega_2)/2$ and $(\omega_1 - \omega_2)/2$, correspond to the ZFS and Zeeman splitting, respectively (the signs flip past the ground-state anticrossing). The real-time feedback signal for magnetic field steps of 35 nT is shown in Fig. 3(d), confirming that the changing magnetic field results only in a change in the linear combination associated with the Zeeman splitting, and no change in the ZFS, which we expect to vary only due to strain. Converting the time-domain feedback signal of the Zeeman splitting to the amplitude spectral density provides a way to quantify the magnetic field sensitivity within some frequency band. This gives a rms magnetic field sensitivity of 4.0 nT/ $\sqrt{\text{Hz}}$ near dc frequencies, resulting in a nearly order of magnitude improvement over, to the best of our knowledge, the next-best sensitivity of magnetometers using the $V/2$ center, which is reported to be 50 nT/ $\sqrt{\text{Hz}}$ [21]. Interestingly, the amplitude spectral density of the ZFS feedback data gives a rms value of 2.3 nT/ $\sqrt{\text{Hz}}$. Although this is not a magnetic sensitivity because the ZFS does not shift with respect to external magnetic fields, this does suggest that the noise limiting the sensitivity of the Zeeman data is likely to be due to environmental magnetic fields. As such, better magnetic isolation from the environment should improve the true magnetic field sensitivity closer to the value obtained with the ZFS data.

An alternative method to simply tracking the change of the ODMR transitions continuously is the use of a pulsed Ramsey sequence [Fig. 4(a)]. The Ramsey pulse scheme creates an evenly weighted superposition of two spin states and lets the phase evolve for some time (τ_{Ram}) before projecting it back, whereupon the spin-population difference is measured. While requiring overhead time for initialization and read-out, the benefit of this method is that the sensitivity is limited by the T_2^* of the transitions and is not affected by power broadening, as in the cw ODMR method. In the case of the $V/2$ center, this method can fully utilize the significantly longer coherence times of the $|-1/2\rangle \rightarrow |1/2\rangle$ transition (3) [29,32]. Working in the $\{1/2, -1/2\}$ basis of the $V/2$ center is complicated by the fact that the off-resonant initialization creates no population difference between the two states and that any induced population difference between states would not directly result in a difference in PL intensity. As such, for Ramsey sequences in the $\{1/2, -1/2\}$ basis, the off-resonant laser is pulsed for 3 μs to initialize the spin state into an equal mixture of $|1/2\rangle$ and $|-1/2\rangle$, after which a rf π -pulse resonant

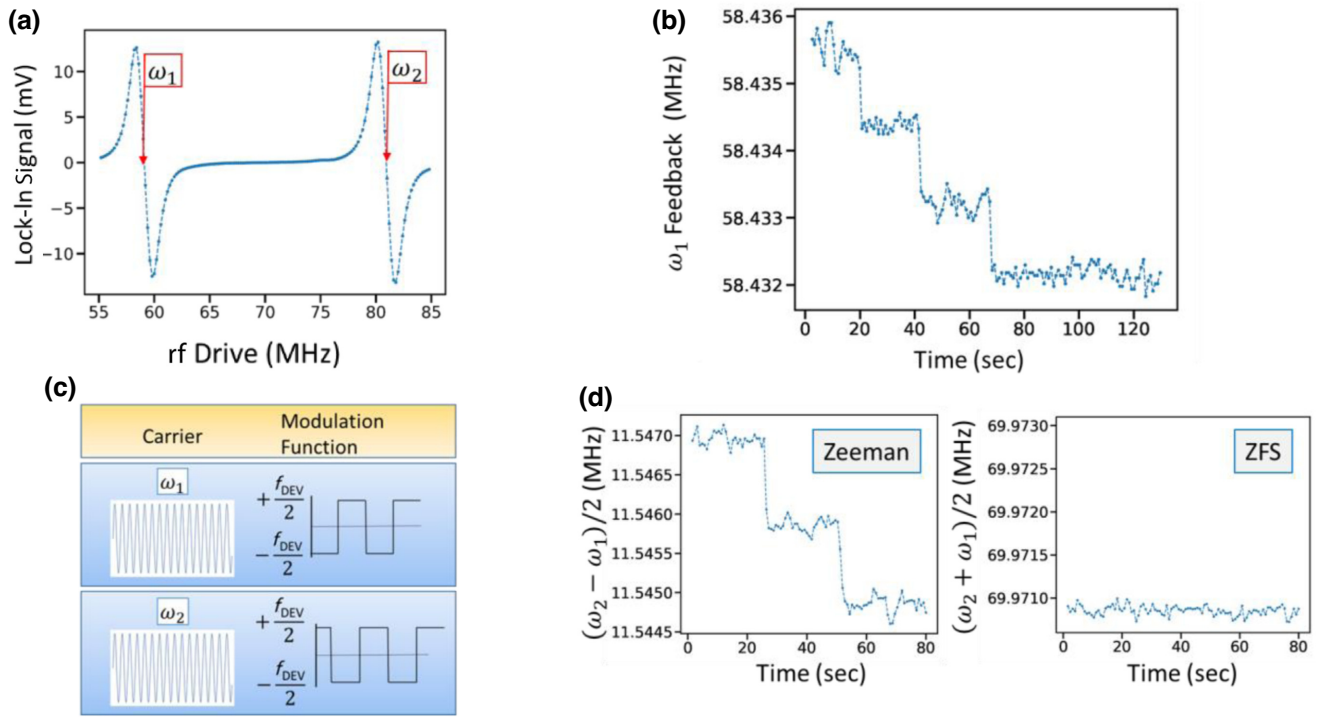


FIG. 3. Real-time feedback for magnetic field sensing. (a) ODMR scan with frequency-modulated rf drives of 3-kHz modulation frequency and 650-kHz deviation frequency. (b) Real-time tracking of transition 1 due to 1- μ A steps in the Helmholtz-coil power supply (corresponding to a magnetic field of 35 nT per step). (c) Two fields for the simultaneous tracking of both transitions. Modulation function between the two is offset by $\Delta\varphi = \pi/2$, meaning the PL signals from transitions 1 and 2 are read out on the X and Y quadratures of the lock-in amplifier independently. (d) Real-time feedback with two-tone rf excitation and 1- μ A step. Left (right) graph corresponds to the linear combination of frequencies, yielding the Zeeman (zero-field) splitting.

to the $| -1/2 \rangle \rightarrow | -3/2 \rangle$ transition creates a population difference between $| 1/2 \rangle$ and $| -1/2 \rangle$. The standard Ramsey pulse sequence runs in the $\{ 1/2, -1/2 \}$ basis before another π -pulse resonant to $| -1/2 \rangle \rightarrow | -3/2 \rangle$ transforms the population difference between $| 1/2 \rangle$ and $| -1/2 \rangle$ into a population difference in $| 1/2 \rangle$ and $| -3/2 \rangle$, which can then be read out as a change in PL intensity. Figure 4(b)

shows a typical, amplitude-modulated Ramsey fringe plot as a function of the free induction delay, τ_{Ram} , with a decay time of $T_2^* = 7.1 \mu\text{s}$ in the $\{ 1/2, -1/2 \}$ basis. For real-time magnetic field tracking, rf source 2, which is resonant with transition 3 is frequency modulated to generate a signal centered around 0 mV. Performing real-time feedback similar to the cw ODMR and converting the time-domain data

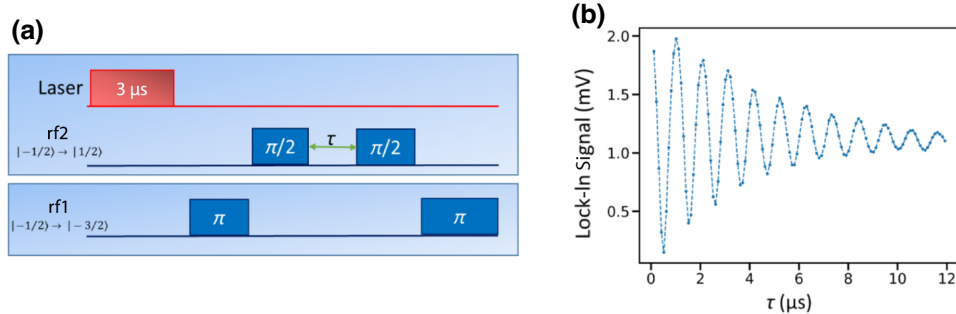


FIG. 4. Magnetic feedback with Ramsey measurement. (a) Pulse sequence for Ramsey interferometry. Laser initializes $| 1/2 \rangle$ into the $\{ -1/2, +1/2 \}$ spin states, while two rf pulses prepare an evenly weighted superposition that precesses for some time τ before a second rf pulse projects it back to an axis, where the difference in spin population can be measured. Preparatory rf pulses at the bottom row are necessary to create and read out a population difference in the $\{ 1/2, -1/2 \}$ basis. (b) Ramsey plot in the $\{ 1/2, -1/2 \}$ basis. Decay rate gives an inhomogeneous dephasing time of $T_2^* = 7.1 \mu\text{s}$.

to an amplitude spectral density again gets the magnetic sensitivity of the measurement near dc frequencies, which is $4.7 \text{ nT}/\sqrt{\text{Hz}}$.

The best magnetic sensitivity of these implementations is limited by the photon shot noise in the detector measuring the PL and is different between the cw ODMR and Ramsey methods. The shot-noise-limited sensitivities for the cw ODMR and Ramsey methods are given, respectively, as [27]

$$\eta_{\text{cw}} = \frac{4}{3\sqrt{3}} \frac{h}{g_e \mu_B} \frac{\Delta\nu}{C_{\text{cw}} \sqrt{R}}, \quad (1)$$

$$\eta_{\text{Ramsey}} = \frac{\hbar}{\Delta m_s g_e \mu_B} \frac{1}{C_{\text{pulse}} e^{-(\tau/T_2^*)} \sqrt{N}} \frac{\sqrt{t_{\text{init}} + \tau + t_{\text{read}}}}{\tau}. \quad (2)$$

Here, $g_e = 2$, μ_B is the Bohr magneton, $\Delta\nu$ is the full width at half maximum of the ODMR lineshape, $C_{\text{cw(pulse)}}$ is the cw (pulsed) ODMR contrast, R (N) is the rate of collected photons per second (per pulse), Δm_s is the spin difference between the two states, τ is the free evolution time, and $t_{\text{init(read)}}$ is the initialization (read-out) time of the Ramsey sequence. Given the values of these parameters for our experiment, we calculate the cw and Ramsey shot-noise-limited sensitivities as $2 \text{ nT}/\sqrt{\text{Hz}}$ and $200 \text{ pT}/\sqrt{\text{Hz}}$, respectively. The experimental cw ODMR sensitivity is within a factor of 2 of the shot-noise limit; this is likely to be limited

by magnetic field noise and laser-amplitude noise. Because transition 3 is as sensitive to these noise sources as either of the transitions used in the cw ODMR measurement, it too is limited near this same sensitivity level, though better magnetic isolation and laser-amplitude noise reduction should lead to an even greater improvement in the case of the Ramsey scheme.

IV. ANGLE-RESOLVED MAGNETOMETRY

Although the $V/2$ center lacks intrinsic vector magnetometry capabilities, it is reported that it can resolve the polar angle of the incident magnetic field from the symmetry axis [31]. This is due to the relatively small 70-MHz ZFS of the defect, which leads to even moderate off-axis magnetic fields mixing the ground-state spin states, resulting in nonsymmetric splitting of transitions 1 and 2. Exploiting the fact that the magnetic field from the CPW is cylindrically symmetric, we modify our setup for spatial scanning to map the y and z components of the magnetic fields generated by a constant current in the 0.5-mm stripline of a CPW [Fig. 5(a)]. The sample and coplanar waveguide are removed from the Helmholtz coil, placed on a 2D translation stage, and a permanent ring magnet above the sample is used to split the degeneracy in the ground state. The cylindrical mirror is removed, as the excitation and collection spot is now normal to the plane of the sample. The CPW is used solely to generate the (test) magnetic

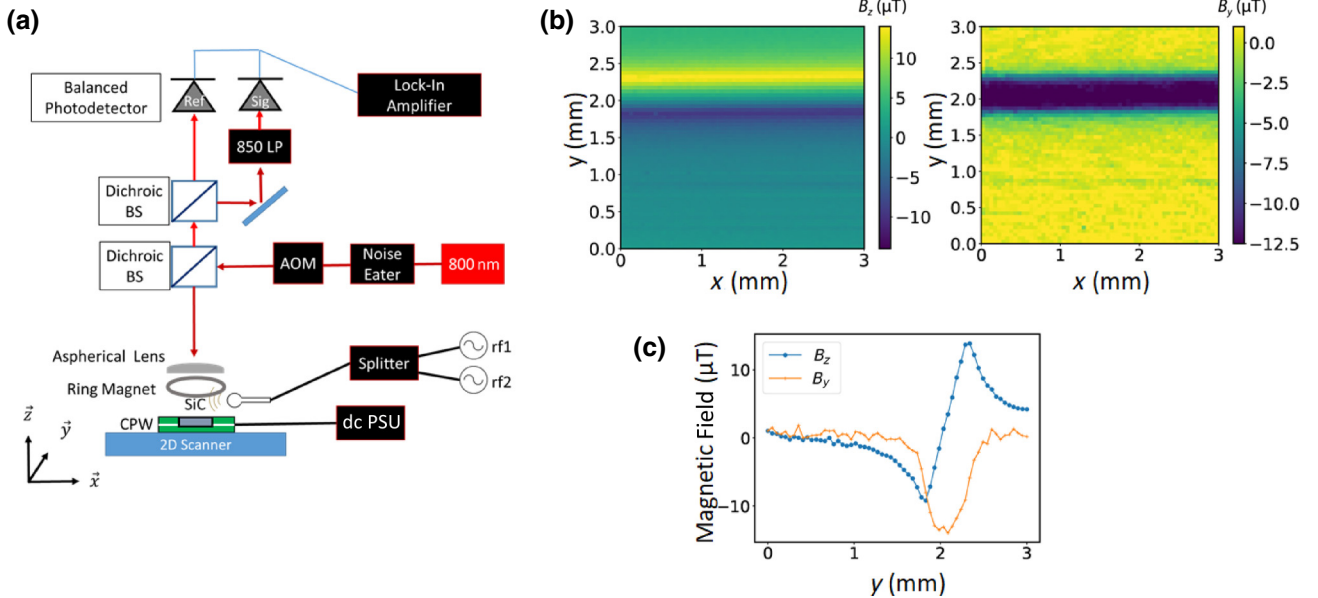


FIG. 5. Angle-resolved magnetometry for imaging of cylindrically symmetric magnetic field. (a) Modifications to the setup in Fig. 2. Of key importance is that the rf driving fields are emitted from a wire antenna, while a steady current flows in the CPW, providing a magnetic field. Both the sample and CPW are fixed to the two-dimensional (2D) scanning stage. CPW with a 0.5-mm stripline is used for increased current density. (b) Solved y and z components of the magnetic field from the 2D array of frequencies resonant to transitions 1 and 2. (c) Vertical slice of data in (b), showing the qualitatively expected results for the magnetic field components around a current-carrying wire.

field from the constant current in the stripline, while a shorted coaxial cable positioned next to the imaging spot is used to emit the rf fields resonant to transitions 1 and 2, which are measured independently, as before (recording two frequencies per pixel in the scan).

A preliminary scan across the part of the sample above the stripline is done with no current present to account for any magnetic field gradients due to the varying distance of the sample from the ring magnet. We repeat this scan after sending 15 mA to the CPW stripline to generate a cylindrically symmetric dc magnetic field. The frequencies of transitions 1 and 2 are determined by the eigenvalues of the Hamiltonian of the $V2$ center with a Zeeman splitting resulting from a B field with two components, B_y and B_z :

$$H/h = DS_z^2 + g\mu_B(B_y\hat{S}_y + B_z\hat{S}_z). \quad (3)$$

The numerical fit gives the values of B_z and B_y at each point in the scan, the spatial map of which is plotted in Fig. 5(b) (after subtracting the fields from the baseline scan). A vertical slice of the magnetic field values of Fig. 5(b) is shown in Fig. 5(c), which agrees well with the qualitative expectations of a straight current-carrying wire, producing a cylindrical magnetic field, with the in-plane component (B_y) being maximal at the stripline center, while the out-of-plane component (B_z) changes sign at the center of the stripline.

The PL intensity in this sensing mode is significantly lower than that in Sec. III due to top-down imaging; as such, the magnetic field sensitivity degrades to 31 nT/ $\sqrt{\text{Hz}}$. The angle resolution can be related to the magnetic sensitivity by solving for transition frequencies 1 and 2 due to an external field, $\vec{B} = (B_0 + B_{\text{test}} \cos \theta)\hat{z} + B_{\text{test}} \sin \theta \hat{y}$, where B_0 is the bias field from the ring magnet and B_{test} is the field to be measured. Propagating the known error in the frequency measurement then gives the angle resolution:

$$\begin{aligned} \eta_\theta &= \eta_v \sqrt{\frac{1}{|\partial v_1/\partial \theta|^2} + \frac{1}{|\partial v_2/\partial \theta|^2}} \\ &= \frac{\eta_B g_e \mu_B}{h} \sqrt{\frac{1}{|\partial v_1/\partial \theta|^2} + \frac{1}{|\partial v_2/\partial \theta|^2}}, \end{aligned} \quad (4)$$

which depends on both B_{test} and θ . For a test field of 10 μT (approximately the field from the CPW), the angle resolution achieves an optimal value of 0.24°/ $\sqrt{\text{Hz}}$ at $\theta = 90^\circ$ but degrades as $\theta \rightarrow 0^\circ$.

V. WIDEBAND AC SENSING

Up to now, we focus on the measurement of nearly dc magnetic fields, with the possibility of extending the bandwidth to a few tens of kHz, given a faster read-out scheme. Fast-magnetic-field targets, such as those present

in microwave circuitry components, need magnetometers sensitive at frequencies far above those considered earlier in this work. For the case of the N- V magnetometer, magnetic fields in the low-MHz regime, as well as near 2.8 GHz, can be measured using Rabi-oscillation-based methods [33,34]. In addition, measurements using intermediate Floquet states can potentially increase the bandwidth of the N- V magnetometer [35]. The $V2$ center is a system uniquely positioned to measure a wide range of frequencies, due to possessing a $|-1/2\rangle \rightarrow |1/2\rangle$ transition, which can be read out with ODMR and tuned from about 10 MHz to 1 GHz with moderate external magnetic fields. The general scheme of ac magnetometry with the $V2$ center is shown in Fig. 6(a). The frequency of transition 3 is tuned into resonance with the frequency of the ac magnetic field to be measured. A Rabi-oscillation pulse sequence is then run continuously with a fixed pulse time, τ_{fixed} , while the lock-in signal is read out. The ac magnetic field of the sensing target serves to change the effective Rabi frequency incident on the ensemble, changing the final spin population at the fixed pulse time.

The setup is brought into the same configuration as that in Fig. 2, with the CPW driving the spin transitions, which are split by the static magnetic field from the Helmholtz coil. Rabi oscillations in the $\{|1/2, -1/2\rangle$ basis are complicated for the same reasons stated earlier for Ramsey sequences, and the standard Rabi pulse sequence must be modified similarly to the Ramsey sequence in Fig. 4(a). A typical Rabi oscillation in the $\{|1/2, -1/2\rangle$ basis, at a 3.5-mT external field, is shown in Fig. 6(b). The decay of the driven Rabi signal is determined primarily by the rf field inhomogeneity across the spin ensemble, because different rf-field projections drive many subensembles at different Rabi frequencies, resulting in an inhomogeneous decay of the Rabi signal. Optimally, the rf pulse needs to be intense enough to strongly pump the entirety of the broadened ensemble (with a linewidth of $\approx 1/\pi T_2^*$) but weak enough to minimize the decay ($T_{2\rho}$) due to rf inhomogeneity. We use the figure of merit from Ref. [33] to quantify the parameters leading to the highest sensitivity for our setup:

$$F(\Omega, \tau) = C(\Omega) e^{-\tau/T_{2\rho}(\Omega)} \frac{\tau}{\sqrt{\tau + t_O}}, \quad (5)$$

where $C(\Omega)$ is the contrast of the Rabi oscillations, τ is the rf-pulse duration, and t_O is the overhead time. We perform scans of the Rabi oscillations at various Rabi frequencies and fit the decaying exponential sinusoid to retrieve the contrast and decay time. Plots of the figure of merit as a function of Ω are shown in Fig. 6(c) for the case of three different transition frequencies (i.e., ac measurement bands) ranging from about 10 MHz to nearly 1 GHz. At low-rf powers, the Rabi frequency is insufficient to drive every defect in the inhomogeneously broadened ensemble,

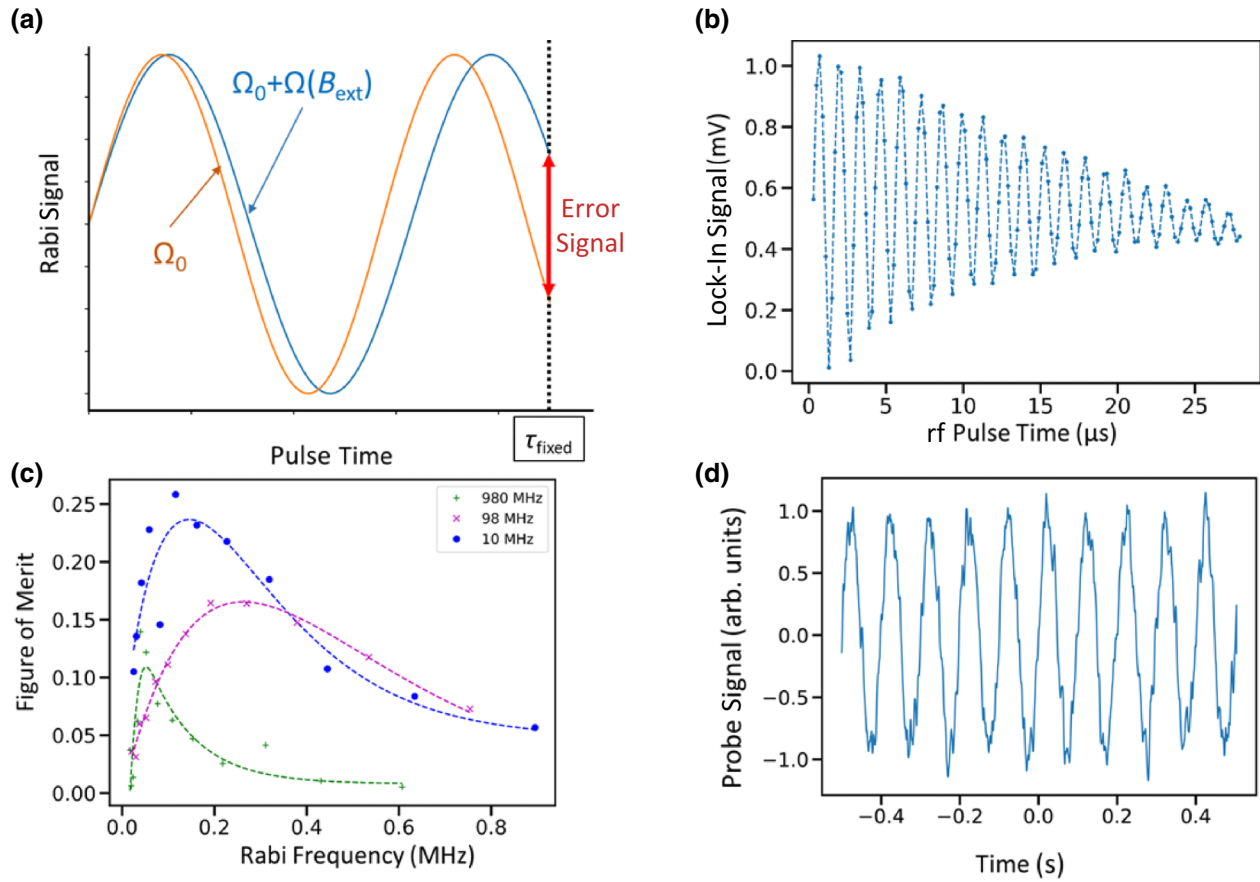


FIG. 6. ac magnetometry using a Rabi pulse scheme. (a) Schematic of ac magnetometry using tracking of the signal from a Rabi oscillation at fixed time. (b) Rabi oscillations in the $\{1/2, -1/2\}$ basis. (c) Figures of merit at three different ac measurement bands as a function of Rabi frequency. Dashed lines are guides to the eye. (d) Read-out of an ac magnetic field at about 100 MHz and amplitude modulated at 10-Hz detuning from the lock-in-detection frequency.

resulting in an overall loss of signal, while higher rf powers increase the decay of the Rabi signal due to the spatial inhomogeneity of the rf drive. Two main factors contribute to the decrease in the figure of merit at higher ac measurement frequencies. First, T_2^* of transition 3 decreases at higher-frequency bands due to either higher spatial inhomogeneity of the magnetic field from the Helmholtz coil or from increased current noise in the coil power supply. Second, the ODMR contrast decreases at high magnetic fields due to its misalignment from the V_2 symmetry axis, resulting in about 15% decrease in the signal.

To generate an ac magnetic field to be probed, we place a shorted coaxial antenna next to the sensing volume and send a rf field at about 100 MHz to the antenna. The frequency of transition 3 is tuned to be in resonance with the coaxial antenna, while the detecting Rabi pulse is chosen to have $\Omega = 130$ kHz and $\tau = 28$ μs to optimize the figure of merit of the detection. To confirm the effects of the rf probe, it is amplitude modulated at a frequency

10 Hz detuned from the modulation frequency of the main rf drive, making it appear as a 10-Hz modulated signal on the lock-in read-out [Fig. 6(d)]. Note that this signal is dependent on the relative phase between the field driving the Rabi oscillations and the external probe. In a practical implementation of this sensing scheme, where the phase of the sensing target is unknown, the measurement will have to be repeated at different phases of the drive field. To quantify the sensitivity, we can convert this real-time noise amplitude from mV to mT with the conversion $\eta_B = \eta_{\text{mV}} \times (\Omega/\kappa \tau) \times (1 \text{ mT}/28 \text{ MHz})$, where η_{mV} is the rms amplitude noise of the lock-in signal and κ is the slope of the linear part of the Rabi oscillation at fixed pulse time τ . The sensitivities at the frequency bands of 13, 101, and 965 MHz are given as 16, 17, and 25 nT/ $\sqrt{\text{Hz}}$, respectively. Although the sensitivity decreases at higher frequencies, we emphasize that this is primarily due to technical limitations of our magnetic and rf-field generation.

VI. OUTLOOK AND CONCLUSIONS

With these sensing modalities demonstrated, future work on this system is expected to focus on improvements of the sensitivity to be more in line with state-of-the-art N-V diamond magnetometers, the sensitivities of which are in the low-pT/ $\sqrt{\text{Hz}}$ range, depending on the frequency band [33,36]. Based on the large difference between the measured Ramsey sensitivity and its corresponding shot-noise limit, we can surmise that environmental magnetic field noise needs to be further suppressed. Laser-amplitude noise is also likely a limiting factor, which can be reduced through laser-power stabilization methods [37] or through a consecutive pulse-subtraction method [33]. A relatively small amount of the available volume of the epilayer is used in the sensing experiment due to optical power restrictions. This optical power restriction can be bypassed in a manner similar to that of diamond magnetometers by coupling the excitation laser from an edge and relying on total internal reflection to increase the volume of initialized defects [38].

In summary, we show magnetometry in isotopically purified silicon carbide using a silicon-vacancy ensemble with a dc field sensitivity of 4.0 nT/ $\sqrt{\text{Hz}}$, an order of magnitude improvement from previous results. A Ramsey-based shot-noise-limited sensitivity of 200 pT/ $\sqrt{\text{Hz}}$ is calculated using our system parameters. Though the V2 ensemble lacks intrinsic vector magnetometry capabilities, the polar angle of the magnetic field can be retrieved in the low-magnetic-field regime, allowing for the imaging of a magnetic target with known cylindrical symmetry. Finally, the existence of a $| -1/2 \rangle \rightarrow | 1/2 \rangle$ spin transition, which is accessible to room-temperature ODMR, enables a highly broadband sensing modality of ac magnetic fields up to GHz frequencies, with sensitivities ranging from 16 to 25 nT/ $\sqrt{\text{Hz}}$. These results position the V2 center as an alternative to the N-V center, which is worthy of further development and refinement due to its unique modalities of sensing and the maturity of silicon carbide as a semiconductor material.

ACKNOWLEDGMENTS

The authors wish to thank Paul Petruzzi from the Laboratory for Physical Sciences for helpful comments. This work is supported by the U.S. Office of Naval Research and the Defense Threat Reduction Agency.

-
- [1] W. E. Bell and A. L. Bloom, Optical detection of magnetic resonance in alkali metal vapor, *Phys. Rev.* **107**, 1559 (1957).
 [2] J. R. Maze, J. M. Taylor, and M. D. Lukin, Electron spin decoherence of single nitrogen-vacancy defects in diamond, *Phys. Rev. B* **78**, 094303 (2008).

- [3] G. Balasubramanian, P. Neumann, D. Twitchen, M. Markham, R. Kolesov, N. Mizuoichi, J. Isoya, J. Achard, J. Beck, J. Tissler *et al.*, Ultralong spin coherence time in isotopically engineered diamond, *Nat. Mater.* **8**, 5 (2009).
 [4] K. Fang, V. M. Acosta, C. Santori, Z. Huang, K. M. Itoh, H. Watanabe, S. Shikata, and R. G. Beausoleil, High-Sensitivity Magnetometry Based on Quantum Beats in Diamond Nitrogen-Vacancy Centers, *Phys. Rev. Lett.* **110**, 130802 (2013).
 [5] M. W. Doherty, N. B. Manson, P. Delaney, F. Jelezko, J. Wrachtrup, and L. C. L. Hollenberg, The nitrogen-vacancy colour centre in diamond, *Phys. Rep.* **528**, 1 (2013).
 [6] J. F. Barry, M. J. Turner, J. M. Schloss, D. R. Glenn, Y. Song, M. D. Lukin, H. Park, and R. L. Walsworth, Optical magnetic detection of single-neuron action potentials using quantum defects in diamond, *Proc. Natl. Acad. Sci. U. S. A.* **113**, 14133 (2016).
 [7] D. Le Sage, K. Arai, D. R. Glenn, S. J. DeVience, L. M. Pham, L. Rahn-Lee, M. D. Lukin, A. Yacoby, A. Komeili, and R. L. Walsworth, Optical magnetic imaging of living cells, *Nature* **496**, 7446 (2013).
 [8] H. C. Davis, P. Ramesh, A. Bhatnagar, A. Lee-Gosselin, J. F. Barry, D. R. Glenn, R. L. Walsworth, and M. G. Shapiro, Mapping the microscale origins of magnetic resonance image contrast with subcellular diamond magnetometry, *Nat. Commun.* **9**, 1 (2018).
 [9] D. B. Bucher, D. R. Glenn, H. Park, M. D. Lukin, and R. L. Walsworth, Hyperpolarization-Enhanced NMR Spectroscopy with Femtomole Sensitivity Using Quantum Defects in Diamond, *Phys. Rev. X* **10**, 021053 (2020).
 [10] D. R. Glenn, D. B. Bucher, J. Lee, M. D. Lukin, H. Park, and R. L. Walsworth, High-resolution magnetic resonance spectroscopy using a solid-state spin sensor, *Nature* **555**, 7696 (2018).
 [11] D. R. Glenn, R. R. Fu, P. Kehayias, D. Le Sage, E. A. Lima, B. P. Weiss, and R. L. Walsworth, Micrometer-scale magnetic imaging of geological samples using a quantum diamond microscope, geochemistry, geophysics, *Geosystems* **18**, 3254 (2017).
 [12] F. Casola, T. van der Sar, and A. Yacoby, Probing condensed matter physics with magnetometry based on nitrogen-vacancy centres in diamond, *Nat. Rev. Mater.* **3**, 1 (2018).
 [13] P. G. Baranov, A. P. Bundakova, A. A. Soltamova, S. B. Orliinskii, I. V. Borovykh, R. Zondervan, R. Verberk, and J. Schmidt, Silicon vacancy in SiC as a promising quantum system for single-defect and single-photon spectroscopy, *Phys. Rev. B* **83**, 125203 (2011).
 [14] S. G. Carter, ÖO Soykal, P. Dev, S. E. Economou, and E. R. Glaser, Spin coherence and echo modulation of the silicon vacancy in 4H-SiC at room temperature, *Phys. Rev. B* **92**, 161202 (2015).
 [15] H. B. Banks, ÖO Soykal, R. L. Myers-Ward, D. K. Gaskill, T. L. Reinecke, and S. G. Carter, Resonant Optical Spin Initialization and Readout of Single Silicon Vacancies in 4H-SiC, *Phys. Rev. Appl.* **11**, 024013 (2019).
 [16] C. P. Anderson, Elena O Glen, Cyrus Zeledon, Alexandre Bourassa, Yu Jin, Yizhi Zhu, Christian Vorwerk, Alexander L Crook, Hiroshi Abe, Jawad Ul-Hassan *et al.*, Five-second coherence of a single spin with single-shot

- readout in silicon carbide, *Sci. Adv.* **8**, eabm5912 (2022).
- [17] W. F. Koehl, B. B. Buckley, F. J. Heremans, G. Calusine, and D. D. Awschalom, Room temperature coherent control of defect spin qubits in silicon carbide, *Nature* **479**, 7371 (2011).
- [18] S. Castelletto, A. Peruzzo, C. Bonato, B. C. Johnson, M. Radulaski, H. Ou, F. Kaiser, and J. Wrachtrup, Silicon carbide photonics bridging quantum technology, *ACS Photonics* **9**, 1434 (2022).
- [19] B.-S. Song, T. Asano, S. Jeon, H. Kim, C. Chen, D. D. Kang, and S. Noda, Ultrahigh- Q photonic crystal nanocavities based on $4H$ silicon carbide, *Optica* **6**, 991 (2019).
- [20] N. T. Son and I. G. Ivanov, Charge state control of the silicon vacancy and divacancy in silicon carbide, *J. Appl. Phys.* **129**, 215702 (2021).
- [21] J. B. S. Abraham, Cameron Gutzsell, Dalibor Todorovski, Scott Sperling, Jacob E. Epstein, Brian S. Tien-Street, Timothy M. Sweeney, Jeremiah J. Wathen, Elizabeth A. Pogue, Peter G. Brereton *et al.*, Nanotesla Magnetometry with the Silicon Vacancy in Silicon Carbide, *Phys. Rev. Appl.* **15**, 064022 (2021).
- [22] H. Kraus, V. A. Soltamov, F. Fuchs, D. Simin, A. Sperlich, P. G. Baranov, G. V. Astakhov, and V. Dyakonov, Magnetic field and temperature sensing with atomic-scale spin defects in silicon carbide, *Sci. Rep.* **4**, 5303 (2014).
- [23] C. J. Cochrane, J. Blacksberg, M. A. Anders, and P. M. Lenahan, Vectorized magnetometer for space applications using electrical readout of atomic scale defects in silicon carbide, *Sci. Rep.* **6**, 37077 (2016).
- [24] D. Simin, V. A. Soltamov, A. V. Poshakinskiy, A. N. Anisimov, R. A. Babunts, D. O. Tolmachev, E. N. Mokhov, M. Trupke, S. A. Tarasenko, A. Sperlich *et al.*, All-Optical dc Nanotesla Magnetometry Using Silicon Vacancy Fine Structure in Isotopically Purified Silicon Carbide, *Phys. Rev. X* **6**, 031014 (2016).
- [25] S. A. Tarasenko, A. V. Poshakinskiy, D. Simin, V. A. Soltamov, E. N. Mokhov, P. G. Baranov, V. Dyakonov, and G. V. Astakhov, Spin and optical properties of silicon vacancies in silicon carbide – a review, *Phys. Status Solidi B* **255**, 1700258 (2018).
- [26] W. Dong, M. W. Doherty, and S. E. Economou, Spin polarization through intersystem crossing in the silicon vacancy of silicon carbide, *Phys. Rev. B* **99**, 184102 (2019).
- [27] J. F. Barry, J. M. Schloss, E. Bauch, M. J. Turner, C. A. Hart, L. M. Pham, and R. L. Walsworth, Sensitivity optimization for NV-diamond magnetometry, *Rev. Mod. Phys.* **92**, 015004 (2020).
- [28] E. Bauch, Swati Singh, Junghyun Lee, Connor A. Hart, Jennifer M. Schloss, Matthew J. Turner, John F. Barry, Linh M. Pham, Nir Bar-Gill, Susanne F. Yelin, and Ronald L. Walsworth, Decoherence of ensembles of nitrogen-vacancy centers in diamond, *Phys. Rev. B* **102**, 134210 (2020).
- [29] I. Lekavicius, R.L. Myers-Ward, D.J. Pennachio, J.R. Hajzus, D.K. Gaskill, A.P. Purdy, A.L. Yeats, P.G. Brereton, E.R. Glaser, T.L. Reinecke, and S.G. Carter, Orders of Magnitude Improvement in Coherence of Silicon-Vacancy Ensembles in Isotopically Purified $4H$ -SiC, *PRX Quantum* **3**, 010343 (2022).
- [30] S.-Y. Lee, M. Niethammer, and J. Wrachtrup, Vector magnetometry based on $S=3/2$ electronic spins, *Phys. Rev. B* **92**, 115201 (2015).
- [31] D. Simin, F. Fuchs, H. Kraus, A. Sperlich, P. G. Baranov, G. V. Astakhov, and V. Dyakonov, High-Precision Angle-Resolved Magnetometry with Uniaxial Quantum Centers in Silicon Carbide, *Phys. Rev. Appl.* **4**, 014009 (2015).
- [32] V. A. Soltamov, C. Kasper, A. V. Poshakinskiy, A. N. Anisimov, E. N. Mokhov, A. Sperlich, S. A. Tarasenko, P. G. Baranov, G. V. Astakhov, and V. Dyakonov, Excitation and coherent control of spin qubit modes in silicon carbide at room temperature, *Nat. Commun.* **10**, 1678 (2019).
- [33] S. T. Alsid, J. M. Schloss, M. H. Steinecker, J. F. Barry, A. C. Maccabe, G. Wang, P. Cappellaro, and D. A. Braje, A Solid-State Microwave Magnetometer with Picotesla-Level Sensitivity, *arXiv:2206.15440*.
- [34] M. Loretz, T. Roskopf, and C. L. Degen, Radio-Frequency Magnetometry Using a Single Electron Spin, *Phys. Rev. Lett.* **110**, 017602 (2013).
- [35] G. Wang, Y.-X. Liu, J. M. Schloss, S. T. Alsid, D. A. Braje, and P. Cappellaro, Sensing of Arbitrary-Frequency Fields Using a Quantum Mixer, *Phys. Rev. X* **12**, 021061 (2022).
- [36] I. Fescenko, A. Jarmola, I. Savukov, P. Kehayias, J. Smits, J. Damron, N. Ristoff, N. Mosavian, and V. M. Acosta, Diamond magnetometer enhanced by ferrite flux concentrators, *Phys. Rev. Res.* **2**, 023394 (2020).
- [37] F. Tricot, D. H. Phung, M. Lours, S. Guérandel, and E. de Clercq, Power stabilization of a diode laser with an acousto-optic modulator, *Rev. Sci. Instrum.* **89**, 113112 (2018).
- [38] H. Clevenston, M. E. Trusheim, C. Teale, T. Schröder, D. Braje, and D. Englund, Broadband magnetometry and temperature sensing with a light-trapping diamond waveguide, *Nat. Phys.* **11**, 393 (2015).

Correction: The affiliation indicator for the seventh author was incorrect and has been fixed. The name of the fifth author was spelled incorrectly and has been fixed.